Journal of Colloid and Interface Science 327 (2008) 216–223

Contents lists available at ScienceDirect

Journal of Colloid and Interface Science

www.elsevier.com/locate/jcis

The effect of shear on colloidal aggregation and gelation studied using small-angle light scattering

Tahereh Mokhtari [a], A. Chakrabarti [a], Christopher M. Sorensen [a,*], Chung-yin Cheng [b], Dennis Vigil [b]

[a] Department of Physics, Kansas State University, Manhattan, KS 66506, USA
[b] Department of Chemical Engineering, Iowa State University, Ames, IA 50011, USA

ARTICLE INFO

Article history:
Received 8 April 2008
Accepted 8 August 2008
Available online 13 August 2008

Keywords:
Light scattering
Shear
Gelation
Superaggregates

ABSTRACT

In situ light scattering measurements were performed to investigate the effect of low shear rates (0.13–3.56 s^{-1}) on an aggregating colloidal system made of 20 nm polystyrene particles. The aggregating system was subjected to a shear for a short period (ca. 33 s) and *only once* at various times after the onset of aggregation. The effect of shear (aggregation kinetics and morphology) was studied both in a *cluster dilute* and in a *cluster dense* regime (see introduction). Our results have shown that shear can enhance the aggregation and gelation. Shear induced growth can yield hybrid superaggregates when the system is dense.

1. Introduction

Irreversible aggregation of small particles can occur due to Brownian diffusion motion [1–4], shear aggregation [5–20], or gravitational forces [21–25]. It is well known that an aggregate subjected to shear stress may undergo structural modification in two ways or possibly with a combination of both. If there is a weak bond in the structure, it may fracture and break apart; it may then recombine with the same or another aggregate under more favorable conditions, and hence become more compact. On the other hand, shear-induced restructuring occurs when the weak bonds can withstand the stress; however, part of the aggregate may rotate and form more bonds within itself, and hence become more compact.

In previous shear experiments, the effect of shear has been mostly studied in a continuous presence of shear where shear-induced aggregation was dominant over Brownian aggregation during the entire experiment [10,11,13–20]. In these studies, fairly compact aggregates were formed due to shear-induced fragmentation [11,13,15–20], or shear-induced restructuring [14,17]. The fractal dimensions of the aggregates under shear were shown to be either independent of the shear rate in some cases [10,11,13,15,16,18–20] or dependent on the shear rates in other cases in which high shear rates caused higher fractal dimensions [9,14,17]. The fractal dimension of the aggregates under shear have been shown to range from 1.8–2.8 [9–11,13–20].

This work is focused on studying the effect of relatively low shear rates, ranging from 0.13 to 3.56 s^{-1}, on an aggregating system made of 20 nm polystyrene particles. A series of experiments were performed in which the aggregating system was sheared *only once* for a short period (ca. 33 s). The shear was applied at various times after the onset of aggregation where the aggregating system was either in a *cluster dilute* or in a *cluster dense* regime. A *cluster dilute* regime is defined as when the mean nearest neighbor separation R_{nn} is much greater than the aggregates characteristic size R_g; whereas, in a *cluster dense* regime, R_{nn} is comparable with R_g in an aggregating system [26]. A small-angle light scattering (SALS) technique was used to study the aggregation kinetics and the morphology of the aggregates before applying a shear and after cessation of the shear, up to the gel point.

Unlike previous work, we find no evidence for restructuring or fragmentation due to shear in our experiments. Instead, shear always caused enhanced aggregation when the Péclet number was greater than one. Shear applied far away from the gel point yielded aggregation with a fractal dimension of 1.8. However, near the gel point, in the cluster dense regime, shear induced growth of hybrid superaggregates similar to previous simulations and experiments with flame soot aerosols [27].

2. Experimental

2.1. Sample preparation

The experiments were performed with surfactant-free nearly monodisperse polystyrene latex spheres with a diameter of 20 nm (12–15% coefficient of variance, IDC). Magnesium chloride salt

* Corresponding author. Fax: +1 785 532 6806.
E-mail address: sor@phys.ksu.edu (C.M. Sorensen).

0021-9797/$ – see front matter
doi:10.1016/j.jcis.2008.08.017

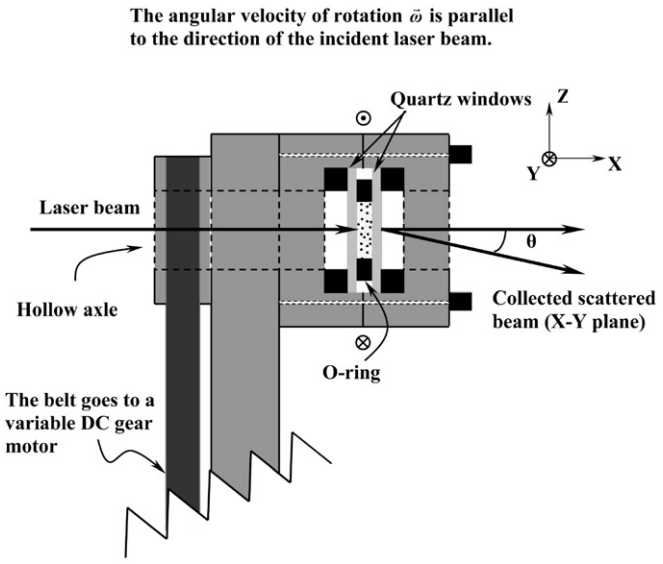

Fig. 1. Schematic side view of the scattering cell and the sample rotator.

($MgCl_2$) was used to screen the double-layer repulsive potential, and hence to induce the aggregation [28]. The polystyrene and $MgCl_2$ solutions were prepared in a 50–50 volume to volume mixture of H_2O and D_2O to match the density of polystyrene (i.e., 1.05 g/cm^3) [29,30], and hence to prevent any sedimentation effects due to gravity [21,22,31]. Equal volumes of polystyrene dispersions and $MgCl_2$ solutions were simultaneously squirted using microliter syringes (Hamilton Company) into a scattering cell (described below). In our experiments, the final volume fraction of polystyrene particles was $f_v = 4.36 \times 10^{-4}$, and the final salt concentration was 10 mM. The mixed solution did not completely fill the cell, and a bubble (ca. 0.14 of the total volume of the cell) was present in the cell.

2.2. Shear cell and shear conditions

The scattering cell, also the shear cell (see Fig. 1), was made of one O-ring (silicone) sandwiched between two 23 mm-diameter quartz windows (NSG Precision Cells, Inc.) and two washers (i.e., to help to seal the sample). The sample was sealed inside a metal sample holder, which had a hole centered on the quartz windows. The optical path length of the scattering cell was 1.8 mm.

After simultaneously squirting the salt and polystyrene solutions into the scattering cell, the cell was immediately mounted onto a sample holder (i.e., sample rotator). The background intensity was then measured after placing the unstable colloidal sample on the sample holder. The background intensity, which was a very small fraction of the scattered intensity, was then subtracted from all subsequent light scattering measurements.

The rotational speed of the sample holder (i.e., scattering cell) was varied from 0.085 to 2.83 rad/s. The axis of rotation of the sample holder, and hence the angular velocity vector ω, was parallel to the direction of the incident laser beam, perpendicular to the windows (see Fig. 1). The rotation rate of the sample holder was varied by altering the voltage of a DC gear motor. All samples were sheared for a short period, 33 ± 3 s (referred to as the shear duration time) and *only once* at various times after the onset of aggregation (referred to as the shear initiation time), typically 1, 2, 3, 5, and 15 min. The shear duration time, which is somewhat arbitrary, was chosen because it was short relative to the gel time yet long enough to cause an effect.

2.3. Shear flow characterization

The average shear rate was characterized by computational fluid dynamics (CFD) simulations using a commercial software, FLUENT 6.2.12 [32]. This program uses the finite volume method to numerically solve the equations of motion and continuity on a computational mesh of user-specified geometry. It also allows the user considerable flexibility to select appropriate options (e.g., rheological models, turbulence closure schemes, boundary conditions, numerical integration schemes, etc.).

Validation of CFD simulation of the behavior of Newtonian fluids has gained widespread acceptance, particularly for simple geometries and low Reynolds numbers. There are numerous cases for which such CFD predictions have been validated. For example, a classical problem is the numerical simulation of a laminar/turbulent Newtonian flow in a square cavity with a moving upper boundary. This case has been studied using different CFD methods and validated against experimental data [33–35]. Other cases with simple geometry similar to the one described in this paper, such as flow around a circular cylinder, also have been shown to be reliable by experimental validation [36]. Many CFD simulations applied to more complicated cases, such as wind tunnel problems [37], have also shown good agreement with experimental data.

In the present case, a computational mesh consisting of 10,770 nodes was constructed to represent the interior and the inside walls of the fluid flow cell. The unsteady equations of motion for laminar Newtonian flow with no slip boundary conditions at the cell walls were integrated using FLUENT's built in variable time step option to minimize error. The presence of the air bubble required the use of a two-phase model. The FLUENT implementation of the volume of fluid scheme [38] was selected for this purpose because of its ability to accurately simulate, with relatively low computational cost, the transport of fluid–fluid interfaces. The integrations were carried out with stagnant fluid initial conditions and were terminated after the calculated velocity fields reached steady state. The computed steady-state velocity fields exhibited simple and intuitive results. In particular, the liquid phase was nearly stagnant in a region approximately intermediate between the bubble–liquid interface and the bottom of the cell, in the plane that bisects the two disks. The magnitude of the fluid velocity increased monotonically as the flow cell walls were approached from this stagnation zone (except of course where the rotational axis intersects the walls).

The volume-averaged shear rate in the liquid phase was computed from the calculated velocity fields excluding a small region near the bubble–liquid interface where the computed shear rate was evidently high because of the large difference between the velocities in the liquid and gas phases. The shear rate averaged over the fluid volume was used because the rotation mixed the sample. Therefore, their shear history should be better represented by the spatial average shear than by simply using the shear rate at the sensing zone of the light scattering experiments. The computed average shear rates, γ, were 0.13, 0.24, 0.48, 0.99, 1.60, 2.61, and 3.56 s^{-1} for rotational speeds of 0.085, 0.17, 0.35, 0.75, 1.26, 2.09, and 2.83 rad/s.

The relative importance of shear-induced aggregation compared to Brownian aggregation in a sheared colloidal dispersion is quantified by a dimensionless quantity referred to as the Péclet number [5,39], which for fractal aggregates we write as

$$\mathrm{Pe} = \frac{R_p^2 \gamma}{D}. \tag{1}$$

In Eq. (1), R_p is the perimeter radius of the aggregates when two clusters collide due to shear, and D is the translational diffusion coefficient given by

$$D = \frac{k_B T}{6\pi\eta R_m}. \quad (2)$$

In Eq. (2), η is the solvent viscosity (as for water $\eta = 8.90 \times 10^{-4}$ kg/ms), k_B is the Boltzmann constant, T is the ambient room temperature ($T = 298$ K), and R_m is the mobility radius of the aggregates. For simplicity, we arbitrarily used the aggregate radius of gyration R_g for both R_p and R_m to determine the Péclet number. Substituting Eq. (2) into Eq. (1) and using R_g in these equations ($R_g \sim R_p \sim R_m$) yields

$$\mathrm{Pe} = \frac{6\pi\eta R_g^3 \gamma}{k_B T}. \quad (3)$$

To estimate Pe with Eq. (3), R_g right before applying a shear was used which was determined via the Guinier analysis (described below). Also, note that for Eq. (3), different authors have used definitions that vary by the numerical constant of 6π (e.g., 3π) [12].

2.4. Small-angle light scattering (SALS) setup

Our SALS setup, similar to that by Ferri [40], is briefly described here. A vertically polarized argon-ion laser (Spectra Physics) operating at a wavelength of $\lambda_o = 488$ nm scattered from the sample. The incident beam had a diameter of 1.25 mm. It entered the sample cell approximately 3 mm below the rotation axis. (Note that the air bubble was ca. 3 mm above the rotation axis and the light scattering experiment was only performed before applying a shear and after the cessation of the shear. Hence, the air bubble did not have an effect on the light scattering measurements.) The light scattered in the horizontal (x–y) plane was then collected by lens L_1 (Achromat $F = 75$ mm, $\phi = 50.8$ mm). The Fourier image formed at the focal plane of L_1 was then conjugated by lens L_2 (Achromat $F = 100$ mm, $\phi = 50.8$ mm) on the detector sensor. A small mirror, made of a drill bit (Gage 73, 0.024 inches diameter) cut and polished at 45°, was placed in the focal plane of the lens L_1. The purpose of the small mirror was to deviate the transmitted beam to ca. 90°, and hence to prevent the unscattered beam from reaching the detector. The detector was a (one-dimensional) N-MOS 512 pixel photodiode array (Hamamatsu). A labview interface program was used for the data acquisition.

The detectable range of the scattering angle, θ, of the SALS setup was between ca. 0.09° and 14° corresponding to the scattering wave vector q ranging between ca. 200 and 31,000 cm^{-1}. We recall that $q = (4\pi/\lambda)\sin(\theta/2)$, where λ and θ are, respectively, the wavelength of the light and the scattering angle in the medium. The refractive index dependence of λ and θ cancel each other in the expansion for q (for small scattering angles and a cell made of two parallel windows). The measurable aggregates' size via this set up ranged approximately from 0.3 to 50 μm.

2.5. Light scattering

The scattered intensity, $I(q)$, of an aggregating system for $q < R_g^{-1}$ (i.e., Rayleigh regime) increases with time as $I(q) \propto n_m N$, where n_m is the initial monomer number density (a constant), and N is the number of monomers per cluster [41]. In an aggregating system, N increases with time resulting in an enhancement of the scattered intensity. Both N and the scattered intensities increase until a space-filling network of fractal clusters forms. Here, the gel time is defined as the time elapsed from the onset of aggregation to the point where there is no further increase in the scattered intensities.

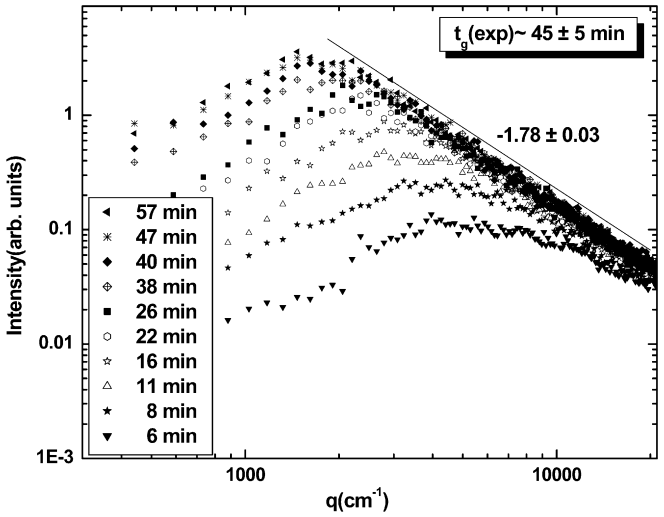

Fig. 2. $I(q)$ (arbitrary units) vs q (cm^{-1}) at different times after the onset of aggregation. The fractal dimension is ca. 1.78 ± 0.03 (i.e., in DLCA regime). The sample gelled at about 45 ± 5 min.

The Guinier regime, where the slope of $I(q)$ vs q goes from 0 to negative, can be used to determine the aggregates' sizes. One can qualitatively obtain the size of the aggregates via $R_g \sim q^{-1}$ in the Guinier regime. However, a more precise analysis should be used to find R_g. This analysis, which is referred to as the Guinier analysis, proceeds by plotting the inverse, normalized scattered intensity, $I(0)/I(q)$ vs q^2. The plot (i.e., $I(0)/I(q) \sim 1 + R_g^2 q^2/3$) should be linear with a slope equal to $R_g^2/3$ when $qR_g < 1$; hence, R_g can be obtained [41–43].

The scattered intensities of an aggregating system follow a power-law behavior $I(q) \sim q^{-D_f}$ for $qR_g > 1$ where D_f is the fractal dimension of the aggregates. Therefore, the fractal dimension can be determined from the slope of the power law region of the log–log plot of $I(q)$ vs q [41].

3. Results and discussions

In order to compare our shear results in terms of the aggregation kinetics and the aggregates' morphology, light scattering measurements of an aggregating system with no shear (i.e., Brownian aggregation) were first carried out which is shown in Fig. 2.

In Fig. 2, $I(q)$ (arbitrary units) is plotted vs q (cm^{-1}) at various times (i.e., 6–57 min) after the onset of aggregation. The sample gelled approximately at 45 ± 5 min (see our definition of the gel time above). The fractal dimension of the aggregating system was $D_f = 1.78 \pm 0.03$, consistent with the DLCA process. There is an apparent peak (at $q \sim 1500$ cm^{-1}) that occurs when R_g becomes comparable in magnitude to the mean nearest neighbor separation of the aggregates, R_{nn} (i.e., *cluster dense* regime) [26,44–47].

Light scattering measurements were then carried out for the shear initiation time of 1 min at various shear rates ranging from 0.13 to 3.56 s^{-1}. The Péclet number (see Eq. (3)) was estimated to be less than one at all shear rates in this range. Fig. 3 shows an example of these measurements.

In Fig. 3, $I(q)$ (arbitrary units) is plotted vs q (cm^{-1}) at various times before initiating the shear, $\gamma = 0.99$ s^{-1}, and after cessation of the shear. It can be seen that the light scattering intensities before applying the shear (at 1 min) are almost negligible. As mentioned earlier, shear was applied for approximately 33 s. After shear was terminated, the scattered intensities did not significantly increase due to shear (see 0.5 min after termination of the shear) compared to that before applying the shear. The sample gelled at approximately 50 ± 10 min, similar to that of the unsheared

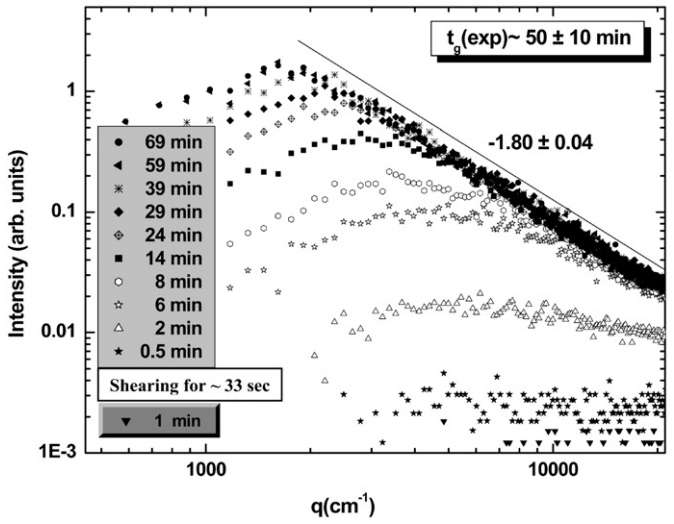

Fig. 3. $I(q)$ (arbitrary units) vs q (cm^{-1}) at different times before applying a shear and after termination of the shear, $\gamma = 0.99\ s^{-1}$. The fractal dimension is 1.80 ± 0.04. The shear initiation time was 1 min. Gelation occurred at about 50 ± 10 min.

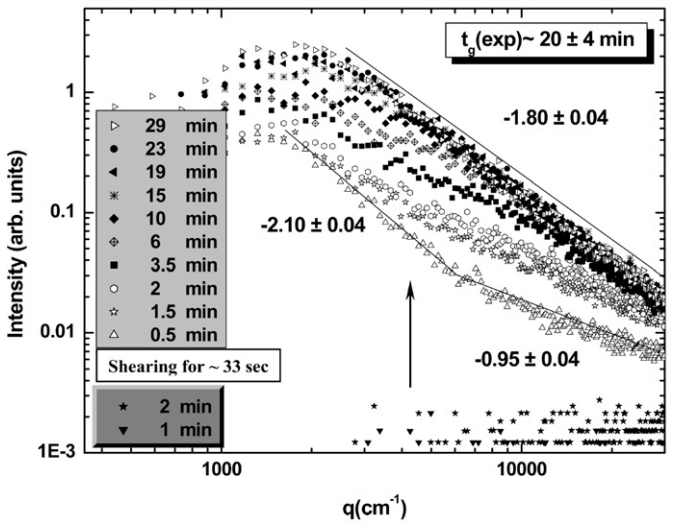

Fig. 4. $I(q)$ (arbitrary units) vs q (cm^{-1}) at different times before applying a shear and after termination of the shear, $\gamma = 2.61\ s^{-1}$. The shear initiation time was ~2 min. Gelation occurred at about 20 ± 4 min. A crossover between two negative slopes of 0.95 ± 0.04 and 2.10 ± 0.04 can be seen, evolving to 1.80 ± 0.04 at the gel point. The arrow indicates the enhanced aggregation due to the shear.

Table 1
Fractal dimension at the gel point, the gel time, and the estimated Péclet number for various shear rates, 0.13 to 3.56 s^{-1}. The shear initiation time was 1 min. The error in the fractal dimension is approximately 0.04

Shear initiation time: 1 min			
γ (s^{-1})	D_f	t_g (min)	Pe
0.13	1.80	40 ± 5	0.01
0.24	1.80	40 ± 5	0.03
0.48	1.80	35 ± 5	0.05
0.99	1.80	50 ± 10	0.11
1.60	1.78	45 ± 10	0.18
2.61	1.80	40 ± 10	0.29
3.56	1.80	45 ± 10	0.39

Table 2
Fractal dimension at the gel point, the gel time, and the estimated Péclet number for the shear initiation time of 5 min at various shear rates ranging from 0.13 to 3.56 s^{-1}. The error in the fractal dimension is approximately 0.03

Shear initiation time: 5 min			
γ (s^{-1})	D_f	t_g (min)	Pe
0.13	1.71	30 ± 5	0.5 ± 0.2
0.24	1.73	25 ± 5	0.6 ± 0.2
0.48	1.75	20 ± 5	0.9 ± 0.2
0.99	1.81	25 ± 5	2.5 ± 0.4
1.60	1.40 & 2.10 evolved to 1.84	15 ± 5	3.5 ± 0.4
2.61	1.40 & 2.10 evolved to 1.83	13 ± 3	8.0 ± 3.0
3.56	1.70 & 2.45	6 ± 1	8.0 ± 1.0

sample. Moreover, the fractal dimension of the gelled sample was $D_f = 1.80 \pm 0.04$ which was again similar, within the uncertainty of the experiments, to that in Fig. 2. A qualitative comparison between Fig. 3 and Fig. 2 (unsheared sample) shows that shear did not cause enhanced aggregation and the aggregates were tenuous similar to a DLCA process. More quantitative analyses (Guinier analyses) will be given later, in the context of Fig. 8 (below), to further support this statement.

In Table 1, the fractal dimension, the gel time, and the estimated Péclet number are shown at various shear rates (0.13–3.6 s^{-1}) when the shear initiation time was 1 min. It can be seen that at all shear rates the gel time is more or less the same as that of an unsheared sample (i.e., $t_g = 45 \pm 5$ min). The fractal dimension also remained ca. 1.80 at these shear rates, similar to that of an unsheared sample. In order to estimate the Péclet number, Eq. (3) was used. At the shear initiation time of 1 min, the size of the aggregates were smaller than the lower limit our SALS size measurements (ca. 300 nm), and hence $R_g = 300$ nm was used to estimate the maximum Péclet number. It can be seen that the Péclet number is smaller than one at all shear rates (see Table 1).

Fig. 4 shows the light scattering measurements ($I(q)$ vs q (cm^{-1})) of a sample sheared 2 min after the onset of aggregation at a relatively high shear rate, $\gamma = 2.61\ s^{-1}$. Here, it should be noted that the intensity of the laser beam was often required to vary from one experiment to the next, and hence the absolute values of the intensities at a certain time should not be compared with those in another figure. It can be seen that applying a shear significantly increased the scattered intensity as depicted by the arrow, and hence indicating a shear enhanced aggregation. Further, two negative slopes of 0.95 ± 0.04 (large q) and 2.10 ± 0.04 (small q) can be seen for the entire range of q implying a hybrid aggregate structure. The negative slope of 0.95 at higher q does not possibly have any quantitative significance as we were limited in our ability to detect the scattering intensity at larger scattering angles. We speculate that the power law regime could have a negative slope of 1.8 at larger q (or smaller length scales) which was beyond our experimental range of detection ($q \sim 31{,}000\ cm^{-1}$). Brownian aggregation gradually *erased* the shear-induced hybrid structure over time up to the gel point. The sample gelled with a more tenuous and homogeneous structure, $D_f = 1.80 \pm 0.04$. The Guinier analyses (described later in the context of Fig. 8, below), showed that the aggregates slightly decreased in size after termination of the shear all throughout the completion of gelation. We call this *post-shear aggregate restructuring*. A rough calculation, however, shows that if these fairly compact $D_f \sim 2.10$ aggregates changed to a more tenuous $D_f \sim 1.80$ aggregates, the aggregate radius of gyration should have become approximately 3 times larger. Our results, however, do not show any increase in the size of aggregates. The disappearance of the double structure is perplexing and remains a question. The sample gelled approximately at $t_g = 20 \pm 4$ min which was shorter than the gel time of the unsheared sample, another evidence for shear-enhanced aggregation.

For the shear initiation time of 5 min, three distinct behaviors based on the shear rates were observed which are described below. Table 2 shows the fractal dimension at the gel point, the gel time, and the estimated Péclet number at these shear rates.

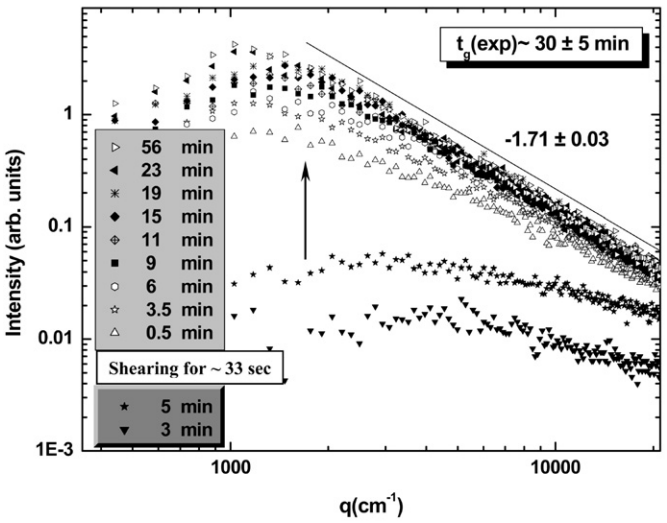

Fig. 5. $I(q)$ (arbitrary units) vs q (cm^{-1}) at different times before applying a shear and after termination of the shear, $\gamma = 0.13\ s^{-1}$. The shear initiation time was 5 min. The sample gelled at about 30 ± 5 min with a fractal dimension of 1.71 ± 0.03. The arrow indicates the enhanced aggregation due to shear.

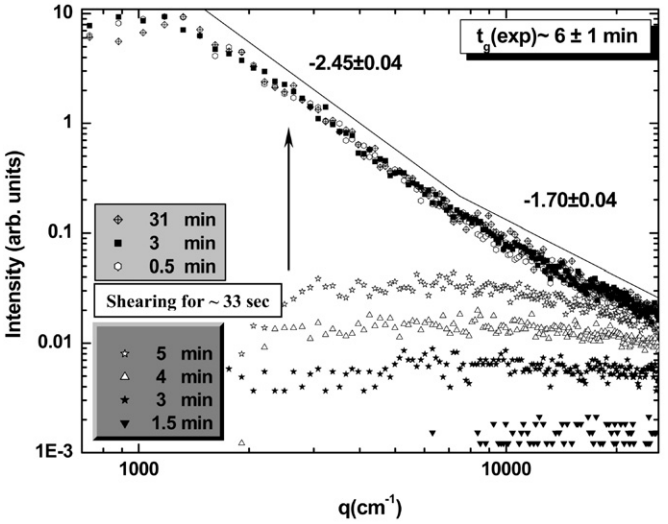

Fig. 6. $I(q)$ (arbitrary units) vs q (cm^{-1}) at different times before applying the shear and after termination of the shear, $\gamma = 3.56\ s^{-1}$. The shear initiation time was 5 min. Gelation occurred at about 6 ± 1 min. A crossover between two negative slopes of 1.70 ± 0.04 and 2.45 ± 0.04 can be seen at the gel point. The arrow indicates the enhanced aggregation due to shear.

At low shear rates ($\gamma \leqslant 0.99\ s^{-1}$), applying a shear enhanced the aggregation. After termination of the shear, aggregation continued via Brownian diffusion motion until the sample(s) gelled with the average fractal dimension of $D_f = 1.75 \pm 0.05$ in this range. The average gel times were approximately 25 ± 5 min, shorter than the gel time of an unsheared sample. The estimated Péclet number at these shear rates (0.13–0.99 s^{-1}) ranged from 0.5 ± 0.2 (at $\gamma = 0.13\ s^{-1}$) to 2.5 ± 0.4 (at $\gamma = 0.99\ s^{-1}$) (see Table 2). Fig. 5 shows an example of this group for the shear rate of $\gamma = 0.13\ s^{-1}$.

At moderate shear rates (1.60 and 2.61 s^{-1}), shear enhanced the aggregation and also caused a hybrid aggregate structure after termination of the shear. Similar to Fig. 4, Brownian aggregation gradually *erased* the hybrid aggregate structure into a uniform structure with the fractal dimension of $D_f = 1.83 \pm 0.03$ at the gel point. The gel time, on average, was 14 ± 4 min, shorter than the gel time at lower shear rates (see above) and of an unsheared sample. The estimated Péclet number at these shear rates (1.60 and 2.61 s^{-1}) was, respectively, 3.5 ± 0.4 and 8.0 ± 3.0 (see Table 2).

Fig. 6 shows the light scattering measurements ($I(q)$ vs q (cm^{-1})) for the highest shear rate, 3.56 s^{-1}. As shown, not only did the shear cause enhanced aggregation, but it also caused the gelation of the sample. The gel time was significantly shorter than that of an unsheared sample, $t_g = 6 \pm 1$ min. The gel had a hybrid aggregate structure with two slopes of -1.75 ± 0.04 (large q) and -2.45 ± 0.04 (small q). The possible mechanism by which these hybrid gel (aggregate) structures were formed is discussed later. The Péclet number was estimated to be ca. 8.0 ± 1.0 (see Table 2).

For the shear initiation time of 15 min, two behaviors were observed which were similar to the cases of low shear rates and high shear rates for the shear initiation time of 5 min. Table 3 shows the fractal dimension at the gel point, the gel time, and the estimated Péclet number at these shear rates.

At low shear rates (i.e., 0.13, 0.24 s^{-1}), shear caused enhanced aggregation; the sample gelled within a few minutes after termination of the shear (similar to Fig. 5) with an average gel time of 17 ± 2 min. The gel had a uniform aggregate structure with a fractal dimension of 1.75 ± 0.04. The estimated Péclet number at these shear rates (0.13 and 0.24 s^{-1}) was, respectively, 3.5 ± 0.5 and 13 ± 1 (see Table 3).

At moderate to high shear rates $\gamma \geqslant 0.48\ s^{-1}$, shear induced a hybrid gel structure. The sample gelled approximately one minute

Table 3
Fractal dimension at the gel point, the gel time, and the estimated Péclet number for the shear initiation time of 15 min at various shear rates ranging from 0.13 to 3.56 s^{-1}. The error in the fractal dimension is approximately 0.04

Shear initiation time: 15 min			
γ (s^{-1})	D_f	t_g (min)	Pe
0.13	1.75	18 ± 2	3.5 ± 0.5
0.24	1.75	16 ± 1	13 ± 1
0.48	1.75 & 2.55	16 ± 1	35 ± 5
0.99	1.75 & 2.55	16 ± 1	20 ± 2
1.60	1.65 & 2.61	16 ± 1	45 ± 5
2.61	1.60 & 2.52	16 ± 1	260 ± 30
3.56	1.73 & 2.45	16 ± 1	150 ± 10

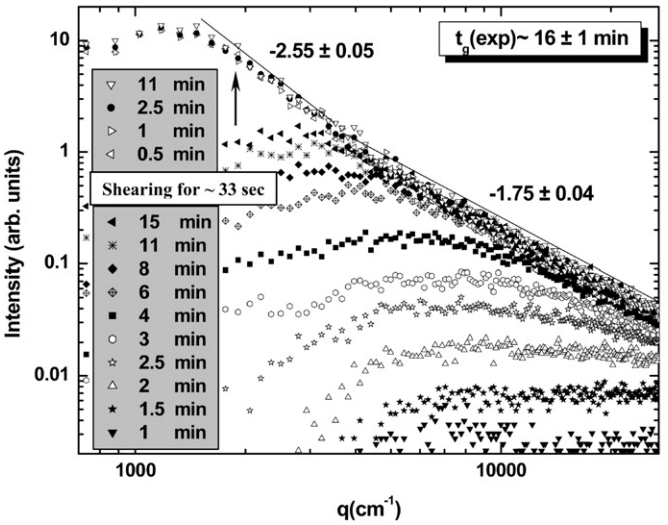

Fig. 7. $I(q)$ (arbitrary units) vs q (cm^{-1}) at different times before applying a shear and after termination of the shear, $\gamma = 0.48\ s^{-1}$. The shear initiation time was 15 min. Gelation occurred at about 16 ± 1 min. A crossover between two negative slopes of 1.75 ± 0.04 and 2.55 ± 0.05 can be seen at the gel point. The arrow indicates the enhanced aggregation due to shear.

past the shear initiation time, $t_g = 16 \pm 1$ min. Fig. 7 shows an example of this group for the shear rate of $\gamma = 0.48\ s^{-1}$. As shown in this figure, shear caused the gelation of the sample, $t_g = 16 \pm 1$ min

(similar to Fig. 6). The gel had a hybrid aggregate structure with two slopes of -1.75 ± 0.04 (large q) and -2.55 ± 0.05 (small q). The estimated Péclet number at these shear rates (0.48–3.56 s^{-1}) was above 20 (see Table 3).

Table 3 shows that the fractal dimensions of the hybrid gel structures are more or less independent of the shear rates once $\gamma \geqslant 0.48$ s^{-1}. This is in contrast with the past work where the fractal dimension at small q (larger length scales) increased with increasing shear [9,14,17]. Furthermore, comparing Tables 3 and 2 suggests that when the aggregating system was in a *cluster dense* regime, a smaller shear rate (0.48 s^{-1} in Table 3) was sufficient to induce a hybrid aggregate structure; whereas in Table 2, a higher shear rate (3.56 s^{-1} in Table 2) was required to cause the same effect.

3.1. Aggregate size characterization

In order to gain a better understanding of the aggregation growth at various shear rates and shear initiation times, the Guinier analysis was used to determine the aggregates' sizes at various times in each experiment. Figs. 8a, 8b, 8c, and 8d, respectively, show these results for the shear rates of 0.13, 0.99, 2.61 and 3.56 s^{-1}. For the shear rates of 2.61 and 3.56 s^{-1}, the analyses for the shear initiation times of 2 and 3 min are shown in addition to the results for the shear initiation times of 1, 5, and 15 min. For comparison same analyses were used to estimate the aggregates' sizes for the unsheared (Brownian aggregation) sample. The uncertainty in determining the aggregates' sizes via Guinier analysis (mentioned above) is represented with the error bars. The horizontal dashed line in Figs. 8a–8d represents the lower limit of our SALS size measurements, ca. 300 nm.

At the shear initiation of 1 min and regardless of the shear rates, the aggregation rate followed more or less the same curve as that for an unsheared sample. At all shear rates, the aggregates' sizes reached a plateau (ca. 4 μm), meaning no further aggregation, approximately at the same time and similar to that for the Brownian aggregation process. At the shear initiation times of 2, 3, 5, and 15 min (Figs. 8a–8d), shear caused enhanced aggregation (see arrows). After cessation of the shear, the system either continued to evolve to the gel point but in a time less than the unsheared case or the shear directly caused gelation (see the plateau region in Figs. 8b–8d at 15 min and Fig. 8d at 5 min). A slightly different trend, on the other hand, can be seen in Fig. 8b at 5 min, Fig. 8c at 2 and 5 min, and Fig. 8d at 3 min. In these cases, after termination of the shear, the aggregates' sizes were initially increased (see arrows), the aggregates were then slightly decreased in size all throughout the completion of gelation. This could be because of the restructuring of the aggregates due to the *Brownian* aggregation. However, note that in all these cases, no hybrid aggregate structure was observed at the gel point.

3.2. Morphology

In order to highlight the effect of shear on the aggregates structures, the light scattering measurements right before initiation of a shear and immediately after termination of the shear shown in Figs. 6 and 7 were replotted in Fig. 9.

Fig. 9a shows the results for the shear initiation time of 5 min and the shear rate of 3.56 s^{-1}. Fig. 9b shows the measurements for the shear initiation time of 15 min and the shear rate of 0.48 s^{-1}. It can be seen that shear enhanced the aggregation (see vertical arrows in Fig. 9) and at the same time (see horizontal arrows in Fig. 9), the aggregates increased in size (smaller q means larger aggregates $R_g \propto 1/q$). This new shear induced structure at small q (larger length scales) has an effective fractal dimension of 2.45 ± 0.04 (a) and 2.55 ± 0.05 (b).

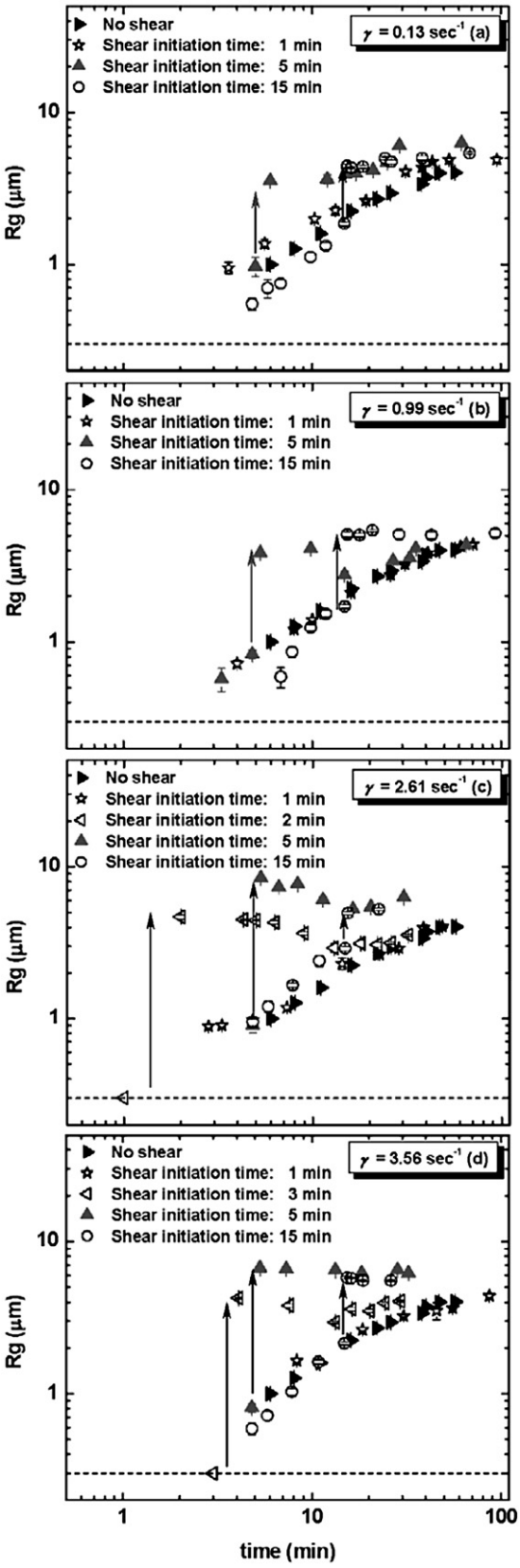

Fig. 8. R_g (μm) vs time for the no shear situation and the shear rates of (a) 0.13 s^{-1}, (b) 0.99 s^{-1}, (c) 2.61 s^{-1}, and (d) 3.56 s^{-1}. The shear initiation time was 1, 5, and 15 min for all shear rates. For shear rates of (c) 2.61 s^{-1} and (d) 3.56 s^{-1}, the analysis for shear initiation times of 2 min and 3 min are also shown, respectively. The horizontal dashed line is the lower limit of our SALS size measurements that is ca. 300 nm. The last data point (plateau region) in each curve represents the gel point. Arrows indicate the enhanced aggregation due to shear.

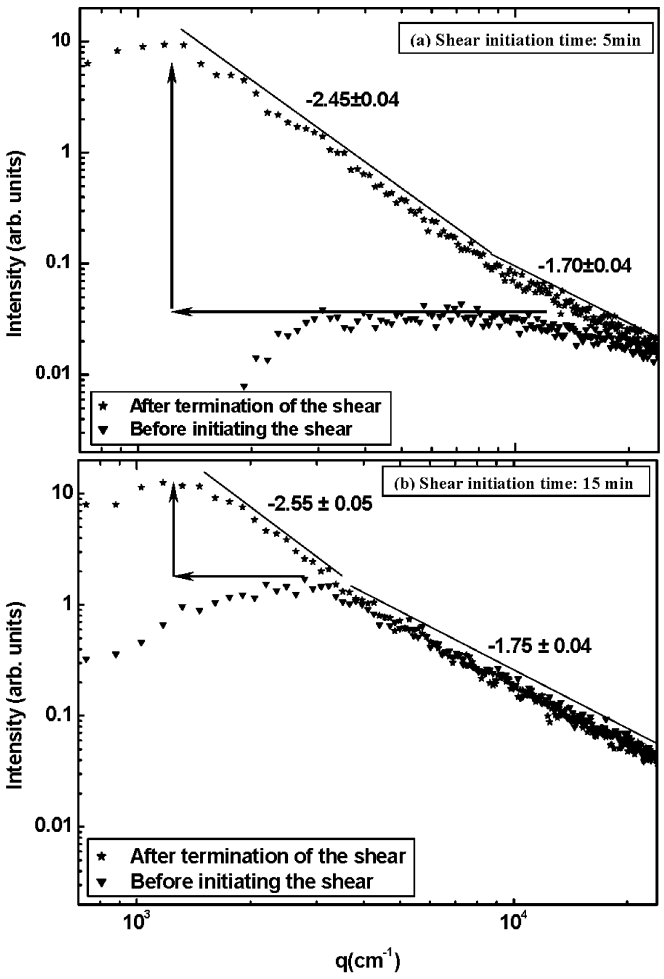

Fig. 9. (a) Light scattering data for the shear initiation time of 5 min and the shear rate of 3.56 s^{-1}, (b) light scattering data for the shear initiation time of 15 min and the shear rate of 0.48 s^{-1}. The arrows show the enhanced aggregation due to shear.

Fragmentation and restructuring have been the only mechanisms by which the effects of shear on aggregating systems have been discussed. As was mentioned earlier for fragmentation, an aggregate subjected to a shear may break apart into smaller aggregates which may then remain tenuous with a fractal dimension identical to an unsheared aggregate [10] or may become more compact as the weaker arms of the aggregate fall off [11,15–20]. However, our results showed no indication of fragmentation. Instead, the aggregate radius of gyration increased, for example, from 500 nm before applying a shear to 8 μm after termination of the shear as shown in Fig. 9a.

It is also well known that an aggregate subjected to a shear may restructure, and hence decrease in size [9,14,17]. In the literature, a hybrid aggregate structure is associated with the restructuring mechanism. The degree of restructuring was shown to depend on the magnitude of the shear rate, meaning that the negative slope at small q (larger length scale) was a function of the shear rate; in other words, the negative slope at small q or larger length scales increased with increasing shear, yielded smaller aggregates' sizes [9,14,17]. In contrast, our results (see Fig. 9) showed that shear caused an increase in the cluster size, not a decrease as expected for restructuring. Moreover, our results (see Table 3 once $\gamma \geqslant 0.48\ s^{-1}$) did not show any increase in the fractal dimension at small q for larger shear rates, but the fractal dimension rather stayed independent of the applied shear rate. Thus, based on both the aggregate size growth and a fractal dimension independent of the applied shear rate, the restructuring mechanism cannot explain our results.

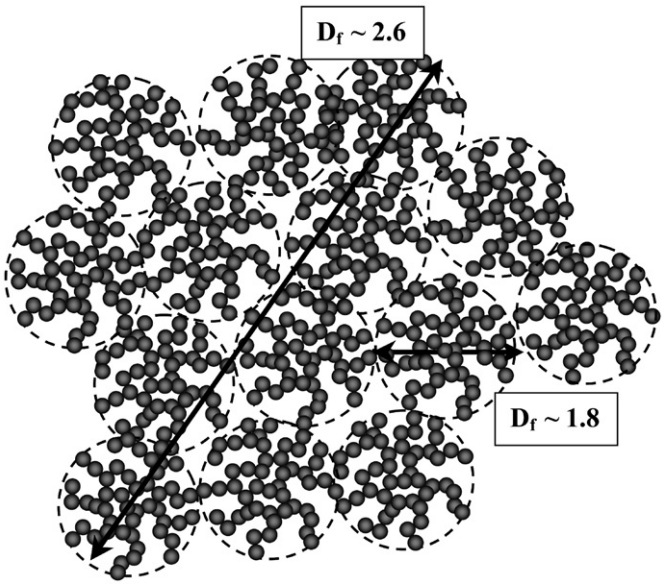

Fig. 10. A schematic drawing of a superaggregate.

In other work from this laboratory, soot aggregates in an acetylene/air laminar diffusion flame were studied using small-angle light scattering [27]. An inhomogeneous aggregate structure was observed at higher heights above the burner orifice (i.e., late aggregation times). Similar to Fig. 9b, Sorensen et al. observed a hybrid aggregate structure with two slopes of −1.8 and −2.6 in their light scattering measurements [27]. They proposed that this hybrid aggregate structure of the flame soot was an indication of superaggregates, a term coined to mean a large aggregate of a given fractal dimension over large length scales composed of smaller aggregates with a different fractal dimension for their smaller length scale [27]. Fig. 10 shows a schematic view of a superaggregate cluster. This proposition was based on a number of simulation works showing that DLCA can proceed forming $D_f \sim 1.8$ fractal aggregates until the system becomes cluster dense [48–50]. Once cluster dense, the aggregation mechanism can crossover to a percolation mechanism which creates superaggregates, with a fractal dimension of $D_f \sim 2.55$ composed of the smaller $D_f \sim 1.8$ DLCA aggregates. The crossover length scale between two negative slopes of 1.8 and 2.55 occurs when the size of the DLCA aggregates reach the radius of gyration at the gel point $R_{g,G}$, [50]. $R_{g,G}$ can be estimated using

$$R_{g,G} = a\left[k_o^{-1}\left(\frac{D_f+2}{D_f}\right)^{3/2} f_v\right]^{1/(D_f-3)} \tag{4}$$

where k_o is the prefactor and in the DLCA regime $k_o \sim 1.3$ [51].

The theoretical $R_{g,G}$ was calculated using the fractal dimensions given in Tables 2 and 3 and the volume fraction used in this work ($f_v = 4.36 \times 10^{-4}$). The experimental $R_{g,G}$ was directly determined from the light scattering measurements when a hybrid aggregate structure was observed. These results are shown in Table 4. A good agreement between theoretical and experimental results was found for the shear initiation time of 15 min (see Table 4). For the shear initiation time of 5 min, there was relatively less agreement between the approximated and the experimental values compared to that for the shear initiation time of 15 min; this could possibly be because in the former case, the system was not as deep into the cluster dense regime, i.e., it was farther from the gel point than at 15 min. Another factor could be that the approximate equation given for $R_{g,G}$ (see Eq. (4)) is greatly de-

Table 4
A comparison between the calculated and the measured $R_{g,G}$ (μm) at shear initiation times of 5 and 15 min

γ (s^{-1})	Shear initiation time 5 min		Shear initiation time 15 min	
	Measured $R_{g,G}$ (μm)	Calculated $R_{g,G}$ (μm)	Measured $R_{g,G}$ (μm)	Calculated $R_{g,G}$ (μm)
0.13				
0.24				
0.48			2.8 ± 0.2	2.5 ± 0.5
0.99			2.0 ± 0.2	2.5 ± 0.5
1.60	1.3 ± 0.1	0.6 ± 0.1	1.9 ± 0.2	1.6 ± 0.3
2.61	1.4 ± 0.2	0.6 ± 0.1	1.3 ± 0.1	1.3 ± 0.2
3.56	1.3 ± 0.1	2.0 ± 0.3	2.2 ± 0.1	2.3 ± 0.4

pendent on any small variation of the fractal dimension. However, overall the theoretical and experimental values are yet satisfactory.

4. Summaries and conclusions

The effect of shear on the structure and the aggregation kinetics of an aggregating polystyrene colloidal system was studied using SALS technique. In our experiments, shear was applied for a short period (ca. 33 s) and only once at various times (1–15 min) after the onset of aggregation. The shear rate ranged between 0.13–3.56 s^{-1}.

When the aggregating system started cluster dilute (when R_{nn} is much greater than R_g) and with a Péclet number less than one, applying a shear did not enhance the aggregation kinetics, leading to a gel structure indistinguishable from that formed via a Brownian DLCA process, $D_f \sim 1.8$. In a cluster dense regime ($R_{nn} \sim R_g$) when the aggregates were big enough to yield a Péclet number greater than one and at low shear rates, shear caused enhanced aggregation; the gel structure, however, was uniform with a fractal dimension of $D_f \sim 1.8$. Also, in a cluster dense regime but at moderate to high shear rates, applying a shear induced a gelation and yielded larger superaggregates with a hybrid structure of $D_f \sim 1.8$ and 2.5. A new feature in which *Brownian* aggregation *erased* the hybrid aggregate structure formed initially due to shear was observed, remains unexplained at this time.

Our experimental results have shown that shear may enhance the aggregation and gelation causing structural modification, not by shear destruction of aggregates (fragmentation or restructuring), but by shear induced growth, a new mechanism by which superaggregates form in a shear field when the system is cluster dense. The fractal dimension of superaggregates was found to be independent of the shear rates applied in our experiments.

Acknowledgment

This research was supported by National Science Foundation grant CTS0403864.

References

[1] M. Kolb, R. Botet, R. Jullien, Phys. Rev. Lett. 51 (1983) 1123–1126.
[2] P. Meakin, Phys. Rev. Lett. 51 (1983) 1119–1122.
[3] M.Y. Lin, H.M. Lindsay, D.A. Weitz, R. Klein, R.C. Ball, P. Meakin, J. Phys. Condens. Matter. 2 (1990) 3093–3113.
[4] M.Y. Lin, H.M. Lindsay, D.A. Weitz, R.C. Ball, R. Klein, P. Meakin, Phys. Rev. A 41 (1990) 2005–2020.
[5] D.L. Swift, S.K. Friedlander, J. Colloid Sci. 19 (1964) 621–647.
[6] G.R. Zeichner, W.R. Schowalter, J. Colloid Interface Sci. 71 (1979) 237–253.
[7] R.C. Sonntag, W.B. Russel, J. Colloid Interface Sci. 113 (1986) 399–413.
[8] T. Hashimoto, T. Takebe, S. Suehiro, J. Chem. Phys. 88 (1988) 5874–5881.
[9] M.Y. Lin, R. Klein, H.M. Lindsay, D.A. Weitz, R.C. Ball, P. Meakin, J. Colloid Interface Sci. 137 (1990) 263–280.
[10] F.E. Torres, W.B. Russel, W.R. Schowalter, J. Colloid Interface Sci. 142 (1991) 554–574.
[11] V. Oles, J. Colloid Interface Sci. 154 (1992) 351–358.
[12] S.M. Clarke, R.H. Ottewill, A.R. Rennie, Adv. Colloid Interface Sci. 60 (1995) 95–118.
[13] P.T. Spicer, W. Keller, S.E. Pratsinis, J. Colloid Interface Sci. 184 (1996) 112–122.
[14] S.J. Jung, R. Amal, J.A. Raper, Powder Technol. 88 (1996) 51–54.
[15] T. Serra, X. Casamitjana, J. Colloid Interface Sci. 206 (1998) 505–511.
[16] T. Serra, J. Colomer, X. Casamitjana, J. Colloid Interface Sci. 187 (1997) 466–473.
[17] C. Selomulya, G. Bushell, R. Amal, T.D. Waite, Langmuir 18 (2002) 1974–1984.
[18] Y. Kikuchi, H. Yamada, H. Kunimori, T. Tsukada, M. Hozawa, C. Yokoyama, M. Kubo, Langmuir 21 (2005) 3273–3278.
[19] L. Wang, D.L. Marchisio, R.D. Vigil, R.O. Fox, J. Colloid Interface Sci. 282 (2005) 380–396.
[20] M. Soos, A.S. Moussa, L. Ehrl, J. Sefcik, H. Wu, M. Morbidelli, J. Colloid Interface Sci. 319 (2008) 577–589.
[21] C. Allain, M. Cloitre, Adv. Colloid Interface Sci. 46 (1993) 129–138.
[22] C. Allain, M. Cloitre, M. Wafra, Phys. Rev. Lett. 74 (1995) 1478–1481.
[23] A.E. Gonzalez, Phys. Rev. Lett. 86 (2001) 1243–1246.
[24] A.E. Gonzalez, J. Phys. Condens. Matter 14 (2002) 2335–2345.
[25] S. Manley, J.M. Skotheim, L. Mahadevan, D.A. Weitz, Phys. Rev. Lett. 94 (2005) 218302.
[26] H. Huang, C. Oh, C.M. Sorensen, Phys. Rev. E 57 (1998) 875–880.
[27] C.M. Sorensen, W. Kim, D. Fry, D. Shi, A. Chakrabarti, Langmuir 19 (2003) 7560–7563.
[28] J. Israelachvili, Intermolecular and Surface Forces, second ed., Academic Press, San Diego, 2006.
[29] M. Carpineti, M. Giglio, Phys. Rev. Lett. 70 (1993) 3828–3831.
[30] L. Cipelletti, S. Manley, R.C. Ball, D.A. Weitz, Phys. Rev. Lett. 84 (2000) 2275–2278.
[31] D. Asnaghi, M. Carpineti, M. Giglio, M. Sozzi, Phys. Rev. A 45 (1992) 1018–1023.
[32] J.C. Tannehill, D.A. Anderson, R.H. Pletcher, Computational Fluid Mechanics and Heat Transfer, second ed., Taylor & Francis, London, 1997.
[33] S.A. Isaev, P.A. Baranov, N.A. Kudryavtsev, D.A. Lysenko, A.E. Usachov, J. Eng. Phys. Thermophys. 78 (2005) 799–816.
[34] S.A. Isaev, P.A. Baranov, N.A. Kudryavtsev, D.A. Lysenko, A.E. Usachov, Thermophys. Aeromech. 12 (2005) 587–608.
[35] S.A. Isaev, P.A. Baranov, N.A. Kudryavtsev, D.A. Lysenko, A.E. Usachov, Thermophys. Aeromech. 13 (2006) 55–65.
[36] R.A. Ahmad, Heat Transfer Eng. 17 (1996) 31–81.
[37] S.A. Isaev, D.A. Lysenko, J. Eng. Phys. Thermophys. 77 (2004) 857–860.
[38] C.W. Hirt, B.D. Nichols, J. Comput. Phys. 39 (1981) 201–225.
[39] D.L. Feke, W.R. Schowalter, J. Colloid Interface Sci. 106 (1985) 203–214.
[40] F. Ferri, Rev. Sci. Instrum. 68 (1997) 2265–2274.
[41] C.M. Sorensen, Aerosol Sci. Technol. 35 (2001) 648–687.
[42] A. Guinier, G. Fournet, Small Angle Scattering of X-Rays, Wiley, New York, 1955.
[43] R. Jullien, J. Phys. I Fr. 2 (1992) 759–770.
[44] J.J. Cerda, T. Sintes, C.M. Sorensen, A. Chakrabarti, Phys. Rev. E 70 (2004) 051405.
[45] M. Carpineti, M. Giglio, Phys. Rev. Lett. 68 (1992) 3327–3330.
[46] A.E. Gonzalez, G. Ramirez-Santiago, Phys. Rev. Lett. 74 (1995) 1238–1241.
[47] P. Poulin, J. Bibette, D.A. Weitz, Europhys. J. B 7 (1999) 277–281.
[48] J.C. Gimel, T. Nicolai, D. Durand, J. Sol-Gel Sci. Technol. 15 (1999) 129–136.
[49] M. Rottereau, J.C. Gimel, T. Nicolai, D. Durand, Europhys. J. E 15 (2004) 133–140.
[50] D. Fry, A. Chakrabarti, W. Kim, C.M. Sorensen, Phys. Rev. E 69 (2004) 061401.
[51] C.M. Sorensen, G.C. Roberts, J. Colloid Interface Sci. 186 (1997) 447–452.